




Exploring the electronic, optical, and thermometric properties of novel AlCuX₂ (X = S, Se, Te) semiconductors: a first-principles study

Merieme Benaadad^{1,*} , Banat Gul², Muhammad Salman Khan³, and Abdelhakim Nafidi¹

¹Laboratory of Condensed Matter Physics and Nano Materials for Renewable Energy, University Ibn Zohr, 80000 Agadir, Morocco

²National University of Sciences and Technology (NUST), Islamabad, Pakistan

³Department of Physics, Abdul Wali Khan University, Mardan 23200, Pakistan

Received: 24 December 2022

Accepted: 16 April 2023

Published online:

29 April 2023

© The Author(s), under exclusive licence to Springer Science+Business Media, LLC, part of Springer Nature 2023

ABSTRACT

In the current study, we investigated the structural, electronic, optical, and thermoelectric properties of three chalcopyrite materials AlCuX₂ (X = S, Se, and Te) employing the full-potential linearized augmented plane waves (FP-LAPW) within the density functional theory (DFT). The generalized gradient approach (GGA-PBE) and the modified Becke–Johnson exchange potential (mBJ-GGA) approximations were employed to calculate the exchange and correlation potentials. The stability of the studied compounds and their structural parameters was evaluated. Our findings revealed that these studied compounds exhibit a semiconductor character with a direct band gap. The two compounds AlCuTe₂ and AlCuSe₂ displayed excellent visible absorption with limited reflectivity. The optical characteristics of the AlCuTe₂ compound better as compared to the AlCuS₂ and the AlCuSe₂ compounds, suggesting it a potential candidate for nonlinear optical applications. The Boltzmann transport theory was employed to analyze the thermoelectric properties. The calculation of Seebeck and hall coefficients confirmed the *p*-type nature in these compounds. According to the thermoelectric results, the AlCuS₂ compound possesses a high electrical conductivity, Seebeck coefficient (*S*), and figure of merit (*ZT*) with low thermal conductivity. The computed results perfectly agree with the reported experimental and theoretical data. Such structures with suitable band gaps can absorb a sufficient amount of light, making them potential candidates for solar cells applications to satisfy energy requirements.

Handling Editor: Kyle Brinkman.

Address correspondence to E-mail: meryaadad@gmail.com

Introduction

One of the major challenges of the twenty-first century is energy issues, because of global resource scarcity and growing energy demand. Renewable energy resources are becoming increasingly popular. Among these resources are sunlight, which can be converted into electricity via the photovoltaic effect. It is one of the most appealing energy pathways for energy production, both in principle and for other reasons such as its vast and inexhaustible availability. As a result, renewable energy resources are rapidly becoming more cost-effective and reliable sources, and their consumption has increased [1, 2]. Over the past several decades, scientific research into the creation of semiconductor materials has advanced significantly with the rise in energy demand. The goal is to make the world more stable by reducing reliance on fossil fuel energy production, which will result in the creation of alternative technologies. Scientists are concentrating their efforts on increasing conversion energy efficiency through the use of durable, abundant, and non-toxic materials, and environmentally friendly, as well as a low-cost manufacturing strategy [3].

Chalcopyrite compounds are attractive materials in the fields of optoelectronics and photonics because of their excellent linear and nonlinear optical and electronic properties. Among these semiconductor materials, we find the family of Cu-III-VI₂ which has been extensively used recently in the research and advancement of new solar cells. The new categories of thin-film solar cell technology have recently made tremendous progress, with an efficiency rate of more than 30% [4], while using ternary chalcopyrite systems, demonstrating promising properties with a radiative limiting performance of 46.7% [5]. Researchers are constantly working to improve the optoelectronic and thermoelectric properties of materials and enhance their effectiveness by varying the fabrication process and by employing a variety of potential compounds. Recently, the ternary chalcopyrite compounds semiconductors with the general formula I-III-VI₂ are among the frequently used alloys for nonlinear optical (NLO) devices, diodes, detectors, thin films, and other applications such as: superconductivity [2], photocatalyst [6], thermoelectricity [7, 8], and spintronic [9–11]. They are distinguished by the emergence of significant absorption in

the near infrared and visible spectrum, where they have a direct band gap, as well as promising chemical, optical, electronic, magnetic, and thermoelectric properties [12–14].

Among this family of chalcopyrite alloys, we found In-based materials such CuInSe₂ (CISe) which is a potential candidate to be employed in different physical, photovoltaic, and technological fields such as thin-film solar cells, because of its promising properties including large optical absorption capacity and conversion efficiency [15]. Even though based CISe thin films are frequently employed as absorber layers in photovoltaic devices, their band gap could be modified by changing In with Ga, Ag, or Al and replacing Se by S or Te [16, 17]. Ag-based groups have also received much interest because of their potential uses in optoelectronics and nonlinear optics. AgGaS₂ and AgGaSe₂ were thoroughly investigated among the Ag-based materials because of their excellent transparency in the wavelength range from 500 to almost 1200 nm and direct band gap transitions [18, 19]. When the vast bulk of the “In” in the CISe film is changed by “Al” and the “Se” element is supplanted by “S”, the resulting band gap of the material can be found in the UV-A region of (320–400 nm) wavelength range. Moreover, a direct band gap transition and wide ultraviolet absorption percentage of over 90% are additional features of CuAlS₂ (CAS) film [20]. Furthermore, CuAlSe₂ is also used frequently as an absorbing material in industrial thin-film solar cells. It has generated wide interest because of its potential uses in UV detectors and multi-junction photovoltaic devices [21, 22].

In general, the review of literature on I-III-VI₂ chalcopyrite ternary alloys has primarily concentrated on sulfides and selenides of wide band gap energies, such as CuInS₂ of 1.53 eV [23], CuGaSe₂ of 1.68 eV [24], AgInS₂ of 1.87 eV [25], and AgGaS₂ of 2.51 eV [26] which have been thoroughly explored for thermoelectric applications. Nevertheless, tellurides with appropriate band gaps, such as CuAlTe₂ and AgAlTe₂, however, have a variety of uses, particularly in photocatalytic and photoelectrochemical (PEC) water splitting [27]. We are aware that understanding the physics of materials necessitates a basic comprehension of their structure, optoelectronic, and thermoelectric properties. We used theoretical approaches known as *ab initio* calculations to enhance our knowledge of the properties of novel AlCuX₂ (X = S, Se, and Te) chalcopyrite alloys. The

scheme allows to describe the physical and chemical properties in the ground state and have appeared as a useful means for exploring various aspects of different class of materials [28–30]. It also enables the describe all the properties in the fundamental state of energy [31, 32]. In terms of computation precision, we for the reason used the Full-Potential Linearized Augmented Plane Wave method [33]. This study is divided into three parts. “Computational details” section describes the computational method. “Results and discussion” section discusses the findings of calculated structural, electronic, optical, and thermoelectric properties of AlCuX₂ (X = S, Se, and Te) compounds. “Conclusion” section presents the conclusion.

Computational details

This study is based on the density functional theory, which has a tendency to establish itself as the norm for electronic structure calculations in the field of materials science because it enables accurate optoelectronic, thermoelectric, and structural predictions [42–44]. The analysis of the physical features of ternary chalcopyrite AlCuX₂ (X = S, Se, Te) materials was analyzed utilizing the all electron full-potential linearized augmented plane wave plus local (FP-LAPW + lo) approach in terms of DFT theory [45, 46] implemented in the WIEN2K code [47, 48]. The precise optimized values of the structural properties were obtained by utilizing GGA-PBE approximation. When exploring the optoelectronic and thermoelectric properties, the SCF cycle was run using the optimized lattice parameters under the influence of the mBJ approximation [49, 50]. The interstitial wave functions, which distinguish between the core and valence states, have been extended into plane waves with a threshold value of $R_{\text{MT}} \times K_{\text{max}} = 7$, where R_{MT} denotes the radius of the smallest Muffin-Tin (MT) spheres while K_{max} indicates the cut-off of plane waves. Structural optimization consists of determining the ground state, and the process of iterations is repeated until the calculation of the total energy converges to less than 10^{-5} Ry. Then, we employed a denser K-mesh of 3000 k-points in the first Brillouin zone (FBZ), which is associated with a $(14 \times 14 \times 14)$ mesh for the density of states calculations (DOS) and the band structure with the generalized gradient approximations of Perdew–Burke–Ernzerhof (GGA-

PBE) and modified Becke–Johnson potential (mBJ). The frequency-dependent complex dielectric function can be employed to examine a system’s linear response to an external electromagnetic field [51]:

$$\varepsilon(\omega) = \varepsilon_1(\omega) + i\varepsilon_2(\omega) \quad (1)$$

Here, $\varepsilon_1(\omega)$ represents photon dispersion, and $\varepsilon_2(\omega)$ denotes the energy absorption of the compounds. The interband contribution to the imaginary part can be computed using the summing transitions from occupied to unoccupied states across the FBZ by the following formula [52]:

$$\varepsilon_2(\omega) = \left(\frac{4\pi^2 e^2}{m^2 \omega^2} \right) \sum_{i,j} \int \langle i|M|j \rangle^2 f_i(1-f_j) \times \delta(E_f - E_i - \omega) d^3k \quad (2)$$

where M indicates the dipole matrix, E_i is the electron energy in the i th state, i and j refer to the initial and final states, respectively, and f_i is the distribution function of Fermi energy for the i th state. The term ‘ ω ’ is the pulsation of the incident light, and k defines the wave vector of the electron concerned by the transition. The Kramers–Kronig relation yields the real component $\varepsilon_1(\omega)$ of the dielectric function [52]:

$$\varepsilon_1(\omega) = 1 + \frac{2}{\pi} P \int_0^{\infty} \frac{\omega' \varepsilon_2(\omega') d\omega'}{\omega'^2 - \omega^2} \quad (3)$$

Here, P represents the principal value and complex shift. Calculating other optical properties require knowing both the real and imaginary parts of the dielectric function, such as the absorption coefficient $I(\omega)$, the energy loss spectrum $L(\omega)$, the refractive index $n(\omega)$, the reflectivity, and the optical conductivity using standard expressions [10]:

$$n(\omega) = \left(\frac{1}{2} \left[\sqrt{(\varepsilon_1^2(\omega) + \varepsilon_2^2(\omega) + \varepsilon_1(\omega))} \right] \right)^{\frac{1}{2}} \quad (4)$$

$$k(\omega) = \left(\frac{1}{2} \left[\sqrt{(\varepsilon_1^2(\omega) + \varepsilon_2^2(\omega) - \varepsilon_1(\omega))} \right] \right)^{\frac{1}{2}} \quad (5)$$

$$R(\omega) = \left| \frac{\sqrt{\varepsilon(\omega)} - 1}{\sqrt{\varepsilon(\omega)} + 1} \right|^2 \quad (6)$$

$$L(\omega) = \frac{\varepsilon_2(\omega)}{\varepsilon_1^2(\omega) + \varepsilon_2^2(\omega)} \quad (7)$$

$$I(\omega) = \frac{\sqrt{2}\omega}{c} (\sqrt{(\varepsilon_1^2(\omega) + \varepsilon_2^2(\omega) - \varepsilon_1(\omega))^{\frac{1}{2}}}) \tag{8}$$

$$\sigma^{real}(\omega) = \frac{\omega}{4\pi} \varepsilon_2(\omega) \tag{9}$$

Results and discussion

Structural properties

The first crucial stage before calculating the material properties is to determine its structural properties. Figure 1 illustrates that AlCuX₂ (X = S, Se, and Te) semiconductors. The three alloys have tetragonal chalcopyrite structure with space group I-42d, and these materials optimized in terms of atomic position accuracy [53]. The GGA-PBE approach is used in the structural study of these compounds to optimize the structural parameters and minimize the structure total energy. The Murnaghan equation of state is used to evaluate the lattice parameters “a” and “b” compressibility modulus (B) and its primitive derivative B’ after optimizing the total energy E of the fundamental state [54]:

$$E(V) = E_0 + \frac{B}{B'(B' - 1)} \left[V \left(\frac{V_0}{V} \right)^{B'} - V_0 \right] + \frac{B}{B'} (V - V_0) \tag{10}$$

Figure 2a–c depicts the variation in total energy of our materials computed according to lattice volume and adjusted using Murnaghan equation of state. Among the three studied materials, the most

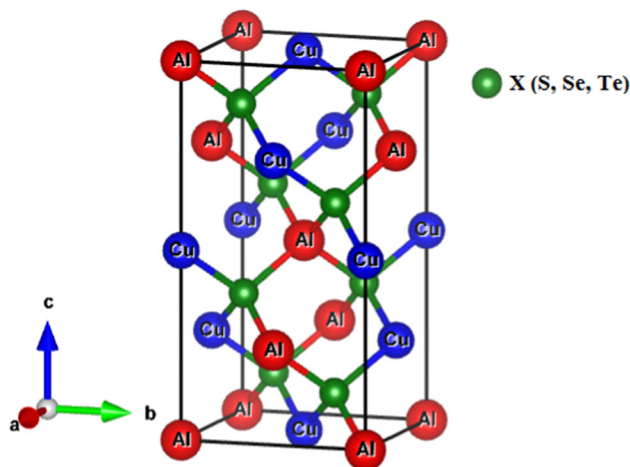


Figure 1 Unit cell for the AlCuX₂ (X = S, Se, Te) materials with the chalcopyrite structures.

stable structure is clearly that one of AlCuTe₂ compound, which has a high-volume value with a low compressibility modulus B compared to the two other materials. For each compound, the calculated structural parameters including the lattice constants (a, c), volume (V₀), total energy (E₀) in fundamental state, and bulk modulus B with its primitive B’ (see Table 1). To facilitate comparison, other experimental and theoretical values are also included. The current findings agree well with the existing data. It observed that the calculated lattice constants for the AlCuX₂ series are in very fine agreement with the other experimental and theoretical calculation, and it increases with increasing atomic number of the anion X from S to Te. The compressibility module decreases as the halogen shifts from S to Te. This shows that as the X anion in AlCuX₂ changes from S to Te, the rigidity of these chalcopyrite increases and they become less compressible and more durable. Therefore, the lattice constants and bulk modulus have an inverse relationship. We used spin-polarized calculations with the PBE-GGA and mBJ potentials to determine the electronic properties of the examined compounds AlCuX₂ (X = S, Se, and Te), including the density of state (DOS) and band structure.

Electronic properties

Examining the electronic structures of compounds enable the determination of their properties and help to clarify the characteristics of solids. This electronic investigation offers a thorough comprehension of the various macroscopic properties of materials. The total density of electronic states (DOS) and the band structure is complementary tools for describing the structure of solids. Figure 3a, b and c represents the electronic band structures according to the high symmetry directions of the first Brillouin zone. As seen in Fig. 3, we notice for these three compounds that the minima of the conduction band and the maxima of the valence band are located at the same point of symmetry of Γ. Therefore, these materials have a direct gap transition in Γ–Γ direction, and that it confirms the semiconductor behavior of our compounds enhancing their effectiveness and functionality in solar cells. Using the GGA-PBE approximation, the E_g values for AlCuS₂, AlCuSe₂, and AlCuTe₂ compounds are 1.75 eV, 0.9 eV, and 1.1 eV, respectively, whereas the mBJ approach improved the band gap values to 2.78 eV, 2.3 eV, and

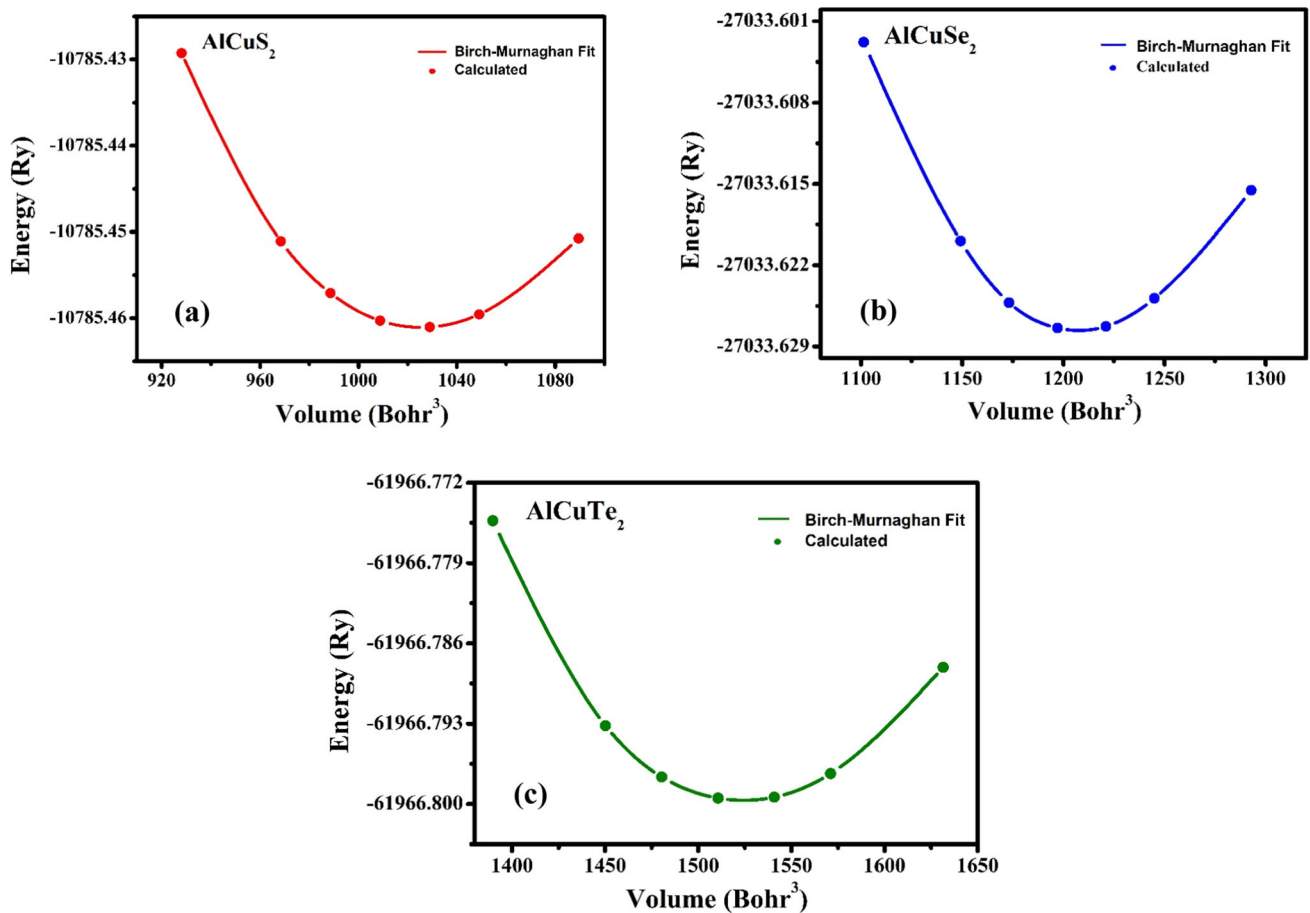


Figure 2 Total-energy versus volume optimization for AlCuX_2 ($X = \text{S, Se, Te}$) compounds.

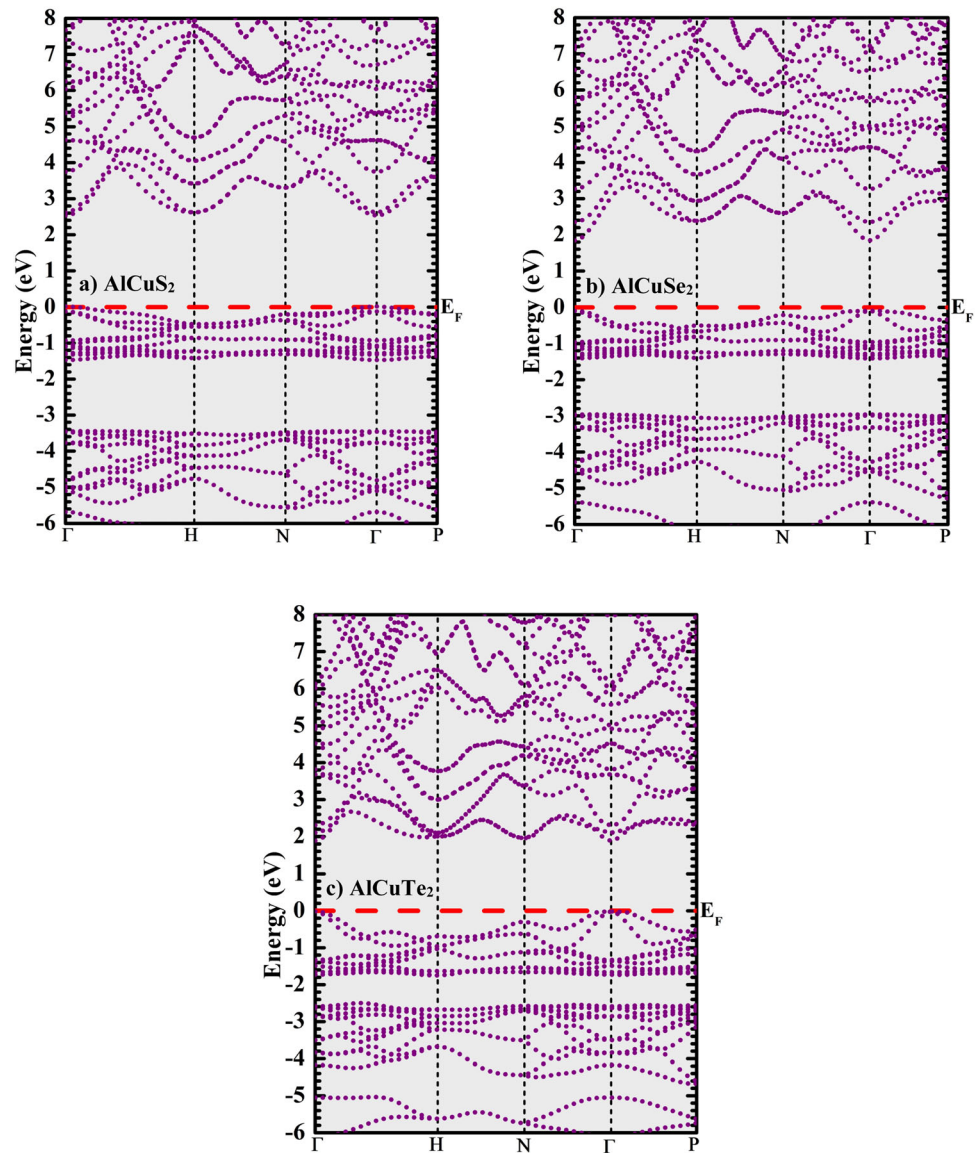
Table 1 Calculated lattice parameters (a and c), volume of the unit cell (V), Bulk modulus B (GPa) and its first pressure derivative B' , and the total energy (E_0) of AlCuX_2 ($X = \text{S, Se, and Te}$) systems

Compound	a (Å)	c (Å)	B (GPa)	B'	V (Å ³)	E_0 (Ry)	Ref
AlCuS ₂	0.5362	1.0660	84.0919	4.6194	291	− 10785.46	This work
	0.5334	1.0444			297		
	0.5321	1.0525			298		
AlCuSe ₂	0.5642	1.1427	66.5823	3.1029	350	− 27033.62	This work
	0.5604				342		
	0.5645	1.1125			354		
AlCuTe ₂	0.5606	1.0902	50.7713	5.3269	448	− 61966.79	This work
	0.6106	1.2141			452		
	0.5964	1.1781			419		
	0.6022	1.2309			446		
	0.6078	1.2068			445		
	0.5964	1.1787			419		

1.1 eV. The summarized results of the current study evaluated by both calculation methods (GGA-PBE and mBJ) can be confirmed (see Table 2) by the preceding theoretical and experimental studies. As compared to other theoretical calculations, our

computed band gap values with mBJ are in very close agreement to the experimentally predicted band gap values. This confirms the accurateness of the used potential in the present study as compared to other potentials. We found that as the anion (X) changes,

Figure 3 Band structures of **a** AlCuS₂, **b** AlCuSe₂, and **c** AlCuTe₂ compounds along the high symmetry directions.



the band gap gets smaller. As a result, in all materials, the anion has played a crucial role in narrowing the electronic band gap. We noticed that the mBJ potential is more efficient to calculate the band gaps of AlCuX₂ (X = S, Se, and Te) compounds than the GGA approach [55].

The calculated total and partial density of states of the three compounds are displayed in Fig. 4a–c. The valence band distinguishes two regions: the first, between 0 and –6 eV, is controlled by the contributions of the Cu-*s*, Cu-*d* and Al-*p* orbitals, in addition to a weak contribution from the *p* states of Al atom. The contribution of the *s* orbital of X (X = S, Se, and Te) and of the *s* orbital of Al dominates the second region between –11 and –12 eV. The

conduction band is clearly controlled by the *p* orbital contribution of Al and Cu, with a minor contribution from the *p* orbital of X, d-X (in the case of X = Se and Te) and a negligible contribution from the *s* orbital of Cu. Theoretical analysis shows that the peaks of the PDOS of the anion X (X = S, Se, Te) are predominant in both conduction and valence band when the anions X (for three compounds) are changed from S to Te. As seen in Fig. 4, the peaks caused by Te atom are more prominent in AlCuTe₂ than they are in AlCuS₂ and AlCuSe₂, which have the anions S and Se, respectively. Band gaps narrow due to the contribution of valence electrons. As a result, we reach the conclusion that Te is crucial in reducing the band gap of AlCuTe₂, which we found to be more practical for

Table 2 Calculated band gaps compared with other experimental and theoretical values (eV) for AlCuX₂ (X = S, Se, Te)

Compounds	E_g (eV)	Method	Ref
AlCuS ₂	2.78	mBJ	This work
	1.75	GGA-PBE	This work
	0.65	PBE	[39]
	1.62	HSE06	[40]
	1.21	mBJ	[40]
	3.49	Exp	[34]
AlCuSe ₂	2.3	mBJ	This work
	0.9	GGA-PBE	This work
	1.53	Exp	[41]
	2.67	Exp	[34]
AlCuTe ₂	1.95	mBJ	This work
	1.1	GGA-PBE	This work
	0.94	LDA	[36]
	2.06	Exp	[37]

maximum visible light absorption than AlCuX₂ (X = S, Se). Consequently, a fundamental understanding of how various anions affect electronic and optical properties was also required. According to the above results, it is obvious that AlCuS₂ with a wide band gap is designed to absorb ultraviolet rays, whereas AlCuSe₂ and AlCuTe₂ are more suited for the absorption of visible rays.

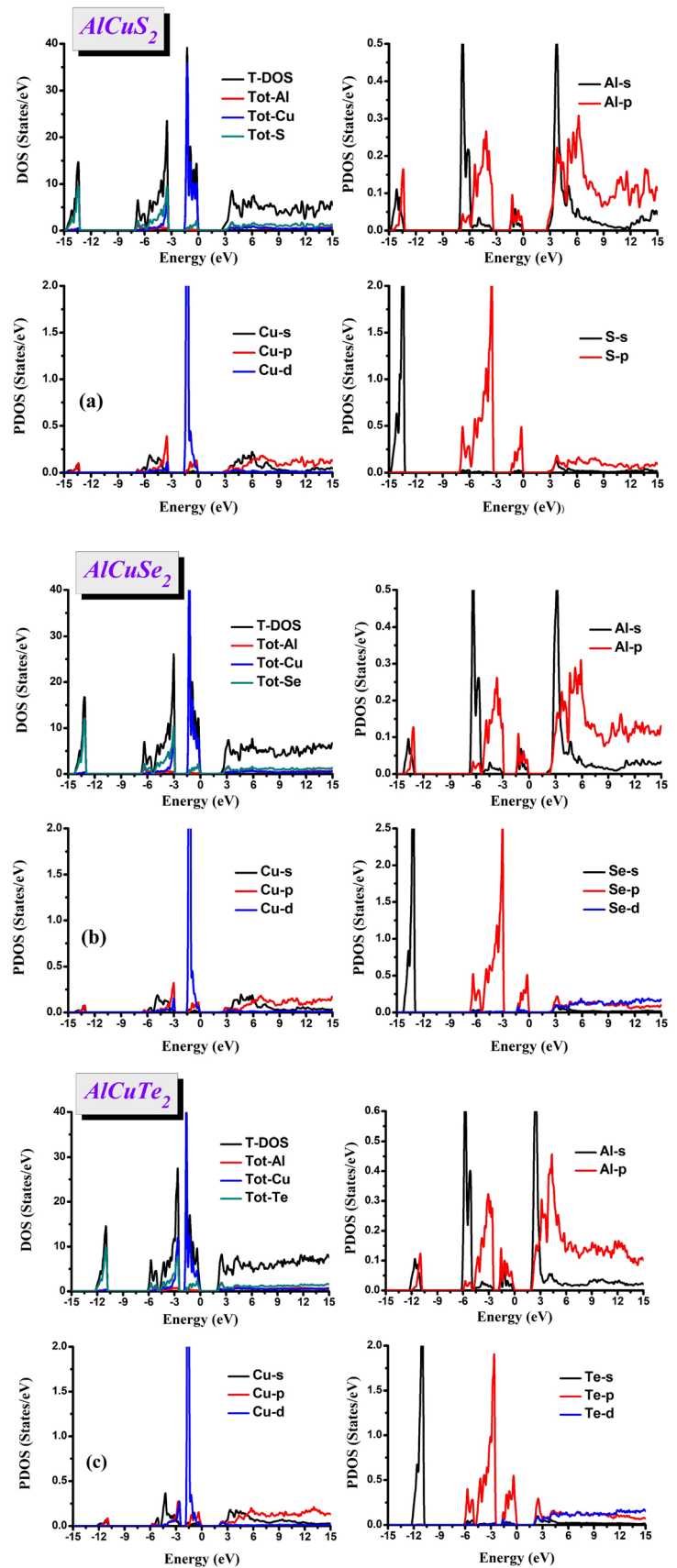
Optical properties

It is important in solid state physics to understand the various methods in which light interacts with material, such as absorption, transmission, reflection, scattering, and emission. That is to say the properties due to the interaction of a solid with an electromagnetic wave of variable frequency. In this section, we studied the different optical properties of the three studied systems. Figure 5a and b represents both parts of the dielectric function, real, and imaginary parts $\epsilon_1(\omega)$ and $\epsilon_2(\omega)$, respectively, versus the energy photons between 0.0 and 14 eV. We mention that the imaginary part attributes the absorption of the system and refers to optical transitions from the valence to conduction bands, while the real part is associated with the polarization of the medium and dispersion of the incident photon. The behavior of $\epsilon_1(\omega)$ is almost identical for the three investigated samples, with variations in static and maximum values. For our compounds, the real part of the dielectric function

begins at zero frequency and tends to increase to its maximum value and then decreases. For $\epsilon_1(0)$, which is attributed to the static dielectric constant $\epsilon_1(\infty)$, the phonon contribution to dielectric screening is ignored. This constant, $\epsilon_1(0)$, is specified with a low energy limit for $\epsilon_1(\omega)$. A narrow band gap was observed, yielding a higher value; the Penn model is an excellent way to explain this proportionality [56]. The $\epsilon_1(0)$ is related to E_g by equation $\epsilon_1(0) \approx 1 + (\hbar\omega_p/E_g)^2$. As a result, for smaller calculated E_g , the $\epsilon_1(0)$ value is greater. The $\epsilon_1^{xx}(0)$ of about 5.32, 6.02, and 7.69 for AlCuS₂, AlCuSe₂, and AlCuTe₂, respectively, and $\epsilon_1^{zz}(0)$ of about 5.43, 6.06, and 7.69 are observed (see Table 3) for AlCuS₂, AlCuSe₂, and AlCuTe₂, respectively, are grouped. The smaller values of $\epsilon_1(0)$ for both alloys resulted from high band gap values and have an inversely proportional relationship. The maximum values of the real components $\epsilon_1^{xx}(\omega)$ and $\epsilon_1^{zz}(\omega)$ are almost the same. Therefore, the maximum value of $\epsilon_1(\omega)$ of 8.68, 9.61, and 12.92 is observed at 3.64 eV, 2.98 eV, and 2.5 eV for AlCuS₂, AlCuSe₂, and AlCuTe₂, respectively. After the second peak and for the three compounds, this real part $\epsilon_1(\omega)$ of the dielectric matrix confirms a reduction and then attains negative values at 7.85, 6.93, and 5.52 eV for AlCuS₂, AlCuSe₂, and AlCuTe₂, respectively. These negative values in this region are mainly due to an extinction coefficient value $k(\omega)$ which is higher than the refractive index $n(\omega)$; $\epsilon_1 = n^2 - k^2$ [Eq. (4) and (5)]. Therefore, it is important to note that these materials have a metallic appearance in these energy intervals, which makes them useful for radiation shielding applications in this energy range.

When we compare the different spectra of the electronic imaginary dielectric function, we realize also that critical points (appearance) in the plots of the different structures are shifted to a lower energy as we move from S to Te, whereas the modification of the anion X has no effect on the value of $\epsilon_2(0)$; it indicates also that $\epsilon_2^{xx}(\omega)$ and $\epsilon_2^{zz}(\omega)$ are anisotropic for the investigated energy range. Correspondingly, the band gap value is the location of the correlating dielectric functions first critical point. This point represents the $\Gamma_v-\Gamma_c$ splitting which specifies the threshold for direct optical transitions from the highest valence band to the lowest conduction band state of AlCuX₂ (X = S, Se and Te). After the band gaps edge, the three materials exhibit a significant

Figure 4 Density of states of a AlCuS_2 , b AlCuSe_2 , and c AlCuTe_2 compounds.



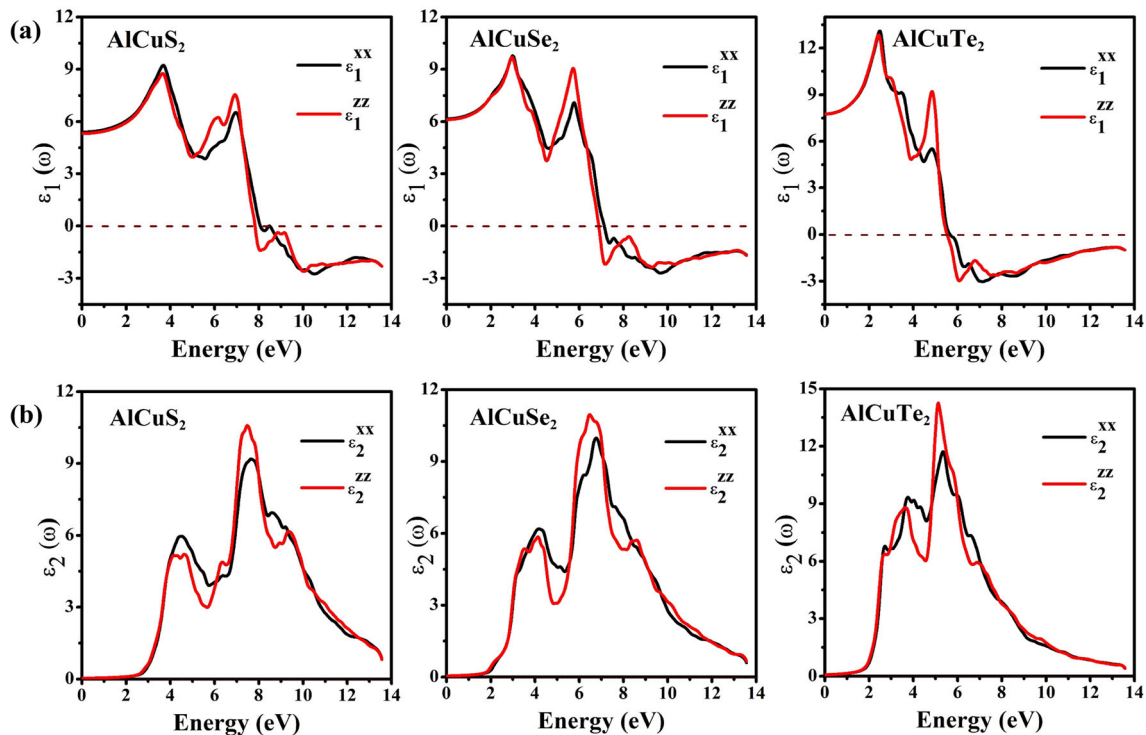


Figure 5 Computed **a** real and **b** imaginary parts of dielectric function of AlCuX_2 ($X = \text{S}, \text{Se}, \text{Te}$) materials.

Table 3 Computed zero frequency limits of static dielectric constant $\epsilon_1(0)$, refractive index $n(0)$, reflectivity $R(0)$ for the studied systems

	AlCuS_2	AlCuSe_2	AlCuTe_2	
$\epsilon_1^{xx}(0)$	5.32	6.02	7.69	This work [36] [58] [59]
			6.9	
			8.26	
			10.9	
$\epsilon_1^{zz}(0)$	5.43	6.06	7.69	
$n^{xx}(0)$	2.29	2.47	2.78	
$n^{zz}(0)$	2.32	2.47	2.78	
$R^{xx}(0)$	0.15	0.17	0.22	
$R^{zz}(0)$	0.16	0.18	0.22	

increase. This is the energy of the absorption edge that causes the significant increase that cuts the energy. These spectra rise quickly because the number of contributing points near the imaginary dielectric part also increases abruptly. The principal peaks that have been observed are located around 10.5 eV, 11.06 eV, and 14.03 eV in the case of AlCuS_2 , AlCuSe_2 , and AlCuTe_2 , respectively, for both $\epsilon_2^{xx}(\omega)$ and $\epsilon_2^{zz}(\omega)$. The high peaks can be described by

significant phonon absorption. As a result, in the visible area of solar cell spectrum, AlCuTe_2 exhibits greater and larger absorption with a maximum of 6.68 at 2.7 eV when compared to AlCuS_2 and AlCuSe_2 alloys. As a consequence, this material is a potentially useful material for solar energy applications, which include solar cell manufacturing. We noted also that the imaginary part of the dielectric function displays a main peak in the ultraviolet region for the three systems. After this maximum value, the imaginary part decreases rapidly with increasing photon energies for the three samples.

The refractive index determines how much light is reflected after it reaches the interface of material. Figure 6a and b shows the refractive index $n(\omega)$ and the optical reflectivity spectra $R(\omega)$. The corresponding static values of the refractive index (see Table 3) are mentioned. The spectral components of the refractive index show a maximum value at 3.68 eV, 5.83 eV, and 2.5 eV for AlCuS_2 , AlCuSe_2 , and AlCuTe_2 , respectively. We observe that dispersion is more significant in the visible area, particularly for AlCuSe_2 and AlCuTe_2 . The high value of reflectivity is about 0.73 (73%), 0.71 (71%), and 0.67 (67%) for AlCuS_2 , AlCuSe_2 , and AlCuTe_2 , respectively. These reflectivity maxima are caused by interband

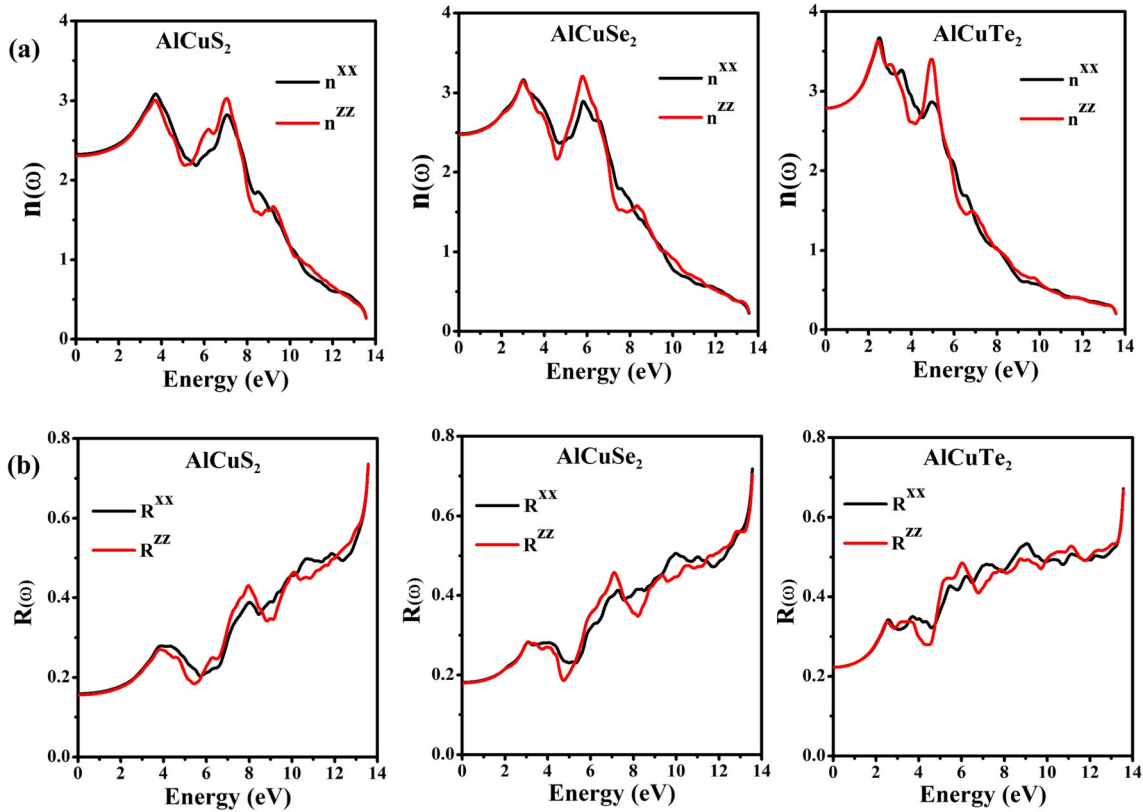


Figure 6 Investigated refractive **a** index and **b** reflectivity of AlCuX_2 ($X = \text{S, Se, Te}$) alloys.

transitions. These peaks occur at 13.5 eV. This value of energy corresponds to $k = 91 \text{ nm}$ (UV region) for the three analyzed materials. In light of this, we reach the conclusion that the three materials can be utilized as UV radiation shielding devices. Additionally, an anisotropy is noted between the range of 6.0 and 12.0 eV in the reflectivity $R^{xx}(\omega)$ and $R^{zz}(\omega)$ spectra for the three compounds.

The absorption coefficient is a fundamental method to characterize the part of the energy absorbed at the interface of the solid. The various interband transitions' absorption curves for the three materials are plotted in Fig. 7a. The absorption starts at 2.8, 2.2, and 1.95 eV for AlCuS_2 , AlCuSe_2 , and AlCuTe_2 , respectively, which agree well with the band gap values of the three systems. Then, the absorption spectra increase to reach the maximum values at 10.5, 9.58, and 8.68 eV for AlCuS_2 , AlCuSe_2 , and AlCuTe_2 , respectively. Figure 7a, shows that the optical absorption for our compounds starts around the values that correspond to the gaps of the materials and increases to reach its maximum value, then decreases with small variations. The extensive absorption range that corresponds to energy values

from visible to ultraviolet demonstrates the utility of these materials for a variety of optoelectronic devices that perform in this energy range, such as solar cells or photovoltaic cells. Figure 7b displays the determined real part of optical conductivity. It begins increasing around the material gap values to its maximum value, then at 7.4 eV, 6.8 eV, and 5.1 eV for AlCuS_2 , AlCuSe_2 , and AlCuTe_2 , respectively, then, decreases with small variations. AlCuS_2 has the highest optical conductivity value in comparison with other compounds in the 6–10 eV energy range.

Furthermore, our calculated energy loss function, $L(\omega)$, and the extension coefficient, $k(\omega)$, are represented in Fig. 8a and b. The energy loss function is much crucial in evaluating the wasted energy of rapid electrons moving in a material. For any of the compounds studied, L does not exhibit any noticeable maxima in the visible and infrared light spectrums. The main peak in the spectra is around 13 eV refers to plasma resonance phenomena, while the associated frequency is defined as plasma frequency [57]. Beyond these identified maximum values, the energy loss function sharply decreases, which correlates with the maximum of reflectivity and the

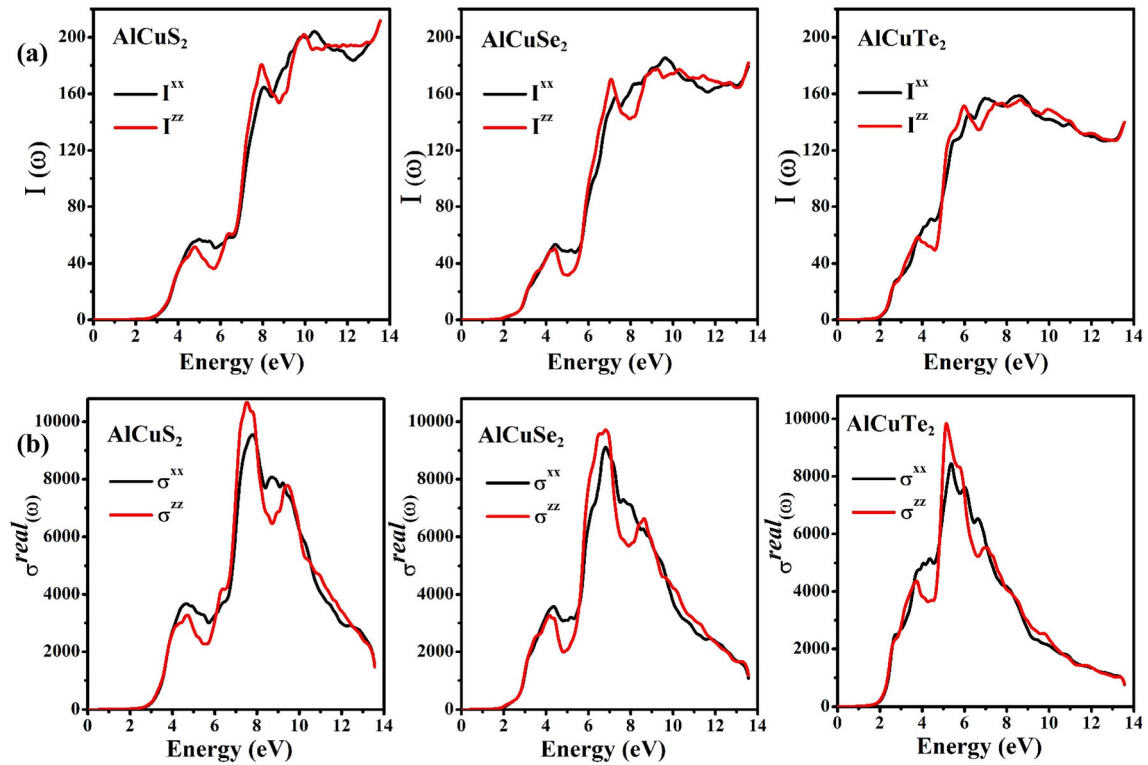


Figure 7 Computed absorption coefficient **a** and optical conductivity **b** of AlCuX_2 ($X = \text{S, Se, Te}$) compounds.

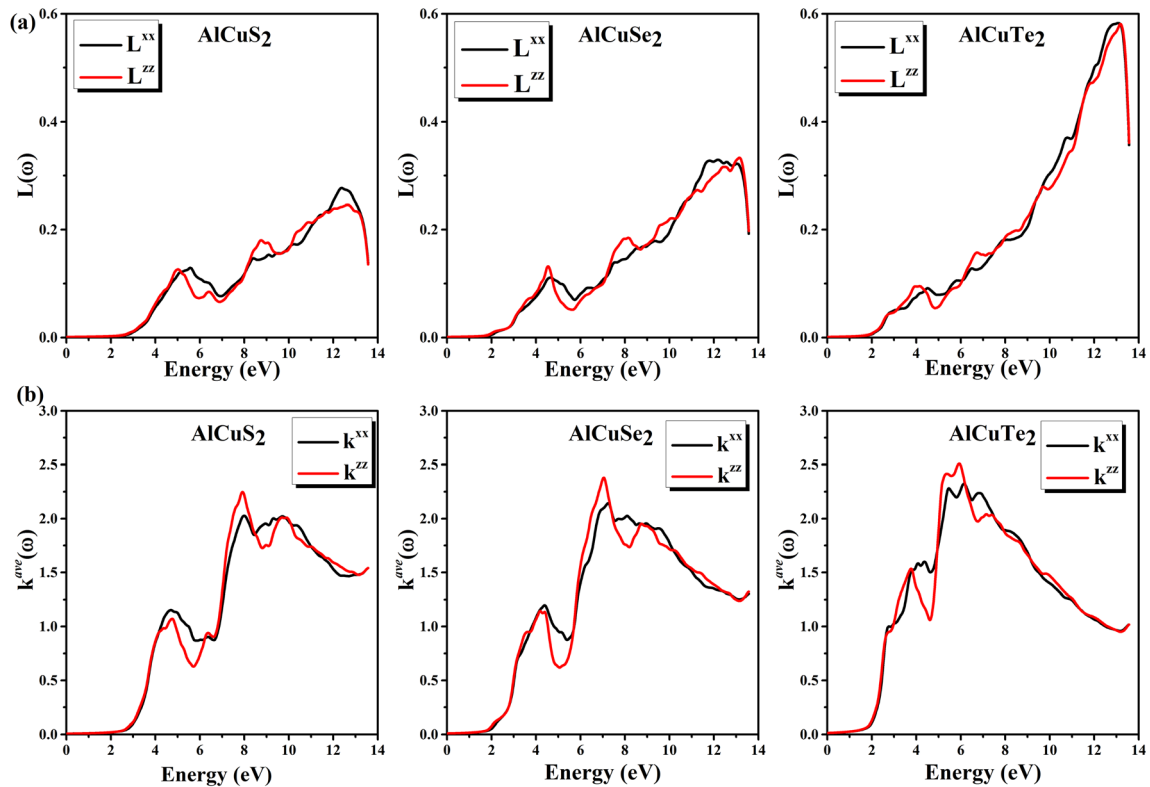


Figure 8 Calculated energy loss function, $L(\omega)$, **a** and extension coefficient, $k(\omega)$ **b** of AlCuX_2 ($X = \text{S, Se, Te}$) compounds.

refractive static value crossing zero. The extension coefficient, $k(\omega)$, shows several high peaks with energies ranging from 5.0 to 9.0 eV. Additionally, it was discovered that as the energy value increased, the two factors of the refractive index, $n(\omega)$, and the extension coefficient, $k(\omega)$, decreased along the identified energy range. Moreover, we found strong anisotropy between the $k^{xx}(\omega)$ and $k^{zz}(\omega)$ parts in the energy interval of 4.0 eV to 10.0 eV for both materials. The energy at which the extinction coefficient realizes its maximum value is the energy at which the dielectric function's real part equals zero. After this peak, the extinction coefficient decreases rapidly with increasing photon energies for all compounds.

Thermoelectric properties

In this technological era, the global consumption of heat supply and waste has expanded. As a result, in order to satisfy the increasing energy demand, scientists are focusing on converting unwanted heat energy into electrical energy. The main objective of investigating thermoelectric properties is to assess how the analyzed substances behave. The Boltzmann transport equation is used in the BoltzTrap code to analyze thermoelectric properties such as the Seebeck coefficient (S), the figure of merit (ZT), electronic power factor ($S^2\sigma\tau/\tau$), and thermal conductivity (κ_e/τ) at different temperatures based on the semi-classical theory of transport [60]. This code has demonstrated to be an extremely efficient method for computing the thermoelectric and transport properties [61, 62].

The majority carrier type is determined by Seebeck coefficients, which have an opposite correlation with electrical conductivity. As shown in Fig. 9a at low temperatures around 80 K, AlCuTe₂ has the maximum value of S , and the AlCuSe₂ has the second highest value. After 100 K, Seebeck coefficient of all materials rise with temperature increase, reaching maximum values at 600 K (AlCuS₂), 700 K (AlCuSe₂), and 500 K (AlCuTe₂). After attaining these maximums, the temperature increases result in a significant decrease in S of the three compounds, particularly for AlCuTe₂. At room temperature, it is clear that all materials have a high Seebeck coefficient of 167, 141, and 117 μV for AlCuS₂, AlCuTe₂, and AlCuSe₂, respectively. We observe that, up to 800 K, AlCuS₂ exhibits higher Seebeck coefficient evolution than the other studied compounds. At 600 K, S reaches its

maximum value. This can be explained by load carriers' increased mobility. Moreover, the results show that the S is positive for all materials, indicating that they are p type seeing as they possess holes as the majority charge carriers, which concurred with the experimental findings for AlCuTe₂ exhibited p nature conductivity and high resistivity [63] using the closed tube CVD technique. Thermal conductivity is influenced by phonons and electrons. It then depends on the mean free path of charge carriers (electrons or holes) and phonons within the sample. The electronic thermal conductivity (κ_e/τ) of the studied samples against the temperature is displayed in Fig. 9b. It is observed that the thermal conductivity rises exponentially by the temperature being raised for the three materials. It is clear that AlCuSe₂ displays the highest κ_e/τ which can be explained by the fact that this later possesses the highest carrier concentration [64].

A high Seebeck coefficient is required for a high-performance thermoelectric material to efficiently convert a temperature difference into a potential difference (or vice versa) and a low electrical resistivity to limit electrical losses due to the Joule effect. These two parameters combine to form the material's power factor PF, which represents the gross electrical power generated by the material as a result of a temperature difference. Figure 9c illustrated the power factor (PF), $S^2\sigma/\tau$, against temperature. The PF increases with increasing the temperature for the three materials with a high starting value for AlCuTe₂ at 100 K. It is observed that raising the temperature leads to high power factor values for AlCuS₂ compared to others studied materials with a value $5 \times 10^{11} \text{ W/mk}^2\text{s}$ at 900 K.

We have calculated the dimensionless figure of merit, following this expression $ZT = S^2\sigma T/\kappa_e$. It is commonly recognized that increasing the figure of merit results in tremendous performance; however, increasing ZT in semiconductor materials ($ZT \leq 1$) has shown challenges because the variables are interdependent; for example, a decrease in thermal conductivity results in a decrease in electrical conductivity, while S has an inverse correlation with electrical conductivity. Figure 9d shows the ZT versus temperature. When the low temperature occurs, all the compounds almost have the same value of ZT . The figure of merit is determined by the Seebeck coefficient; As a result, an excellent thermoelectric device requires a high Seebeck coefficient besides low

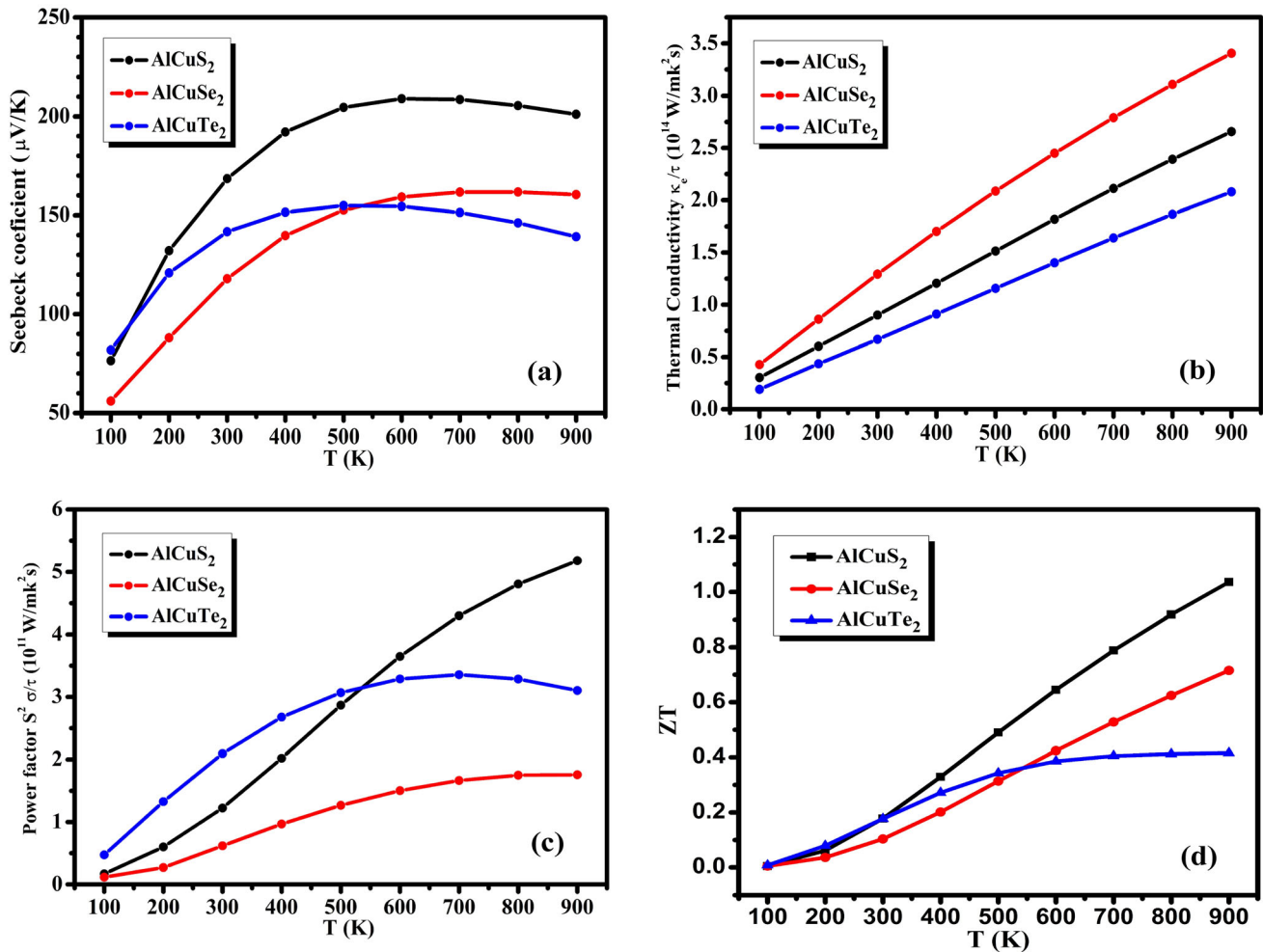


Figure 9 Calculated **a** Seebeck coefficients, **b** thermal conductivity, **c** power factor PF, and **d** figure of merit ZT, of AlCuX₂ (X = S, Se, Te) compounds.

thermal conductivity so that the temperature gradient can be maintained. Indeed, semiconductors materials with ZT close to or greater than 1 (unity) are thought to be attractive thermoelectric device applicants [65, 66]. In our case, starting from room temperature, AlCuS₂ has a high ZT value; at 900 K, its ZT value equals unity. Similarly, AlCuSe₂ has a greater ZT value at high temperatures, implying that these two materials could be potential candidates with high performance for thermoelectricity field. This occurs due to the fact that at the same temperature range, the Seebeck coefficient and electrical conductivity are high (see Fig. 9a), while the electronic thermal conductivity is low (see Fig. 9b). Electrical conductivity ($\sigma = \mu ne$) is related to charge carrier density (n) and mobility (μ), implying that materials with low effective masses have high mobility. As a result, for improved thermoelectric

features, we must achieve a suitable balance of high mobility and reasonable carrier concentration. To reduce the Joule heating effect, materials with high electrical conductivity should be used to design a good thermoelectric device [67].

The electrical conductivity illustrated in Fig. 10a increases with temperature rise for the three materials. AlCuS₂ has a high electrical conductivity value. Figure 10b shows the Hall coefficients. It is clear that all the materials have a positive R_H which confirms the p-type of the investigated materials. Figure 10c displays the variation in specific heats at constant volume C_v with temperature. At low temperatures, it varies as the cube of absolute temperature, which is known as Debye's T^3 law, and at high temperatures, the specific heat value approaches the value given by Dulong and Petit's law ($3R$). It increases with temperature increase following the Dulong–Petits law. The curves then tend

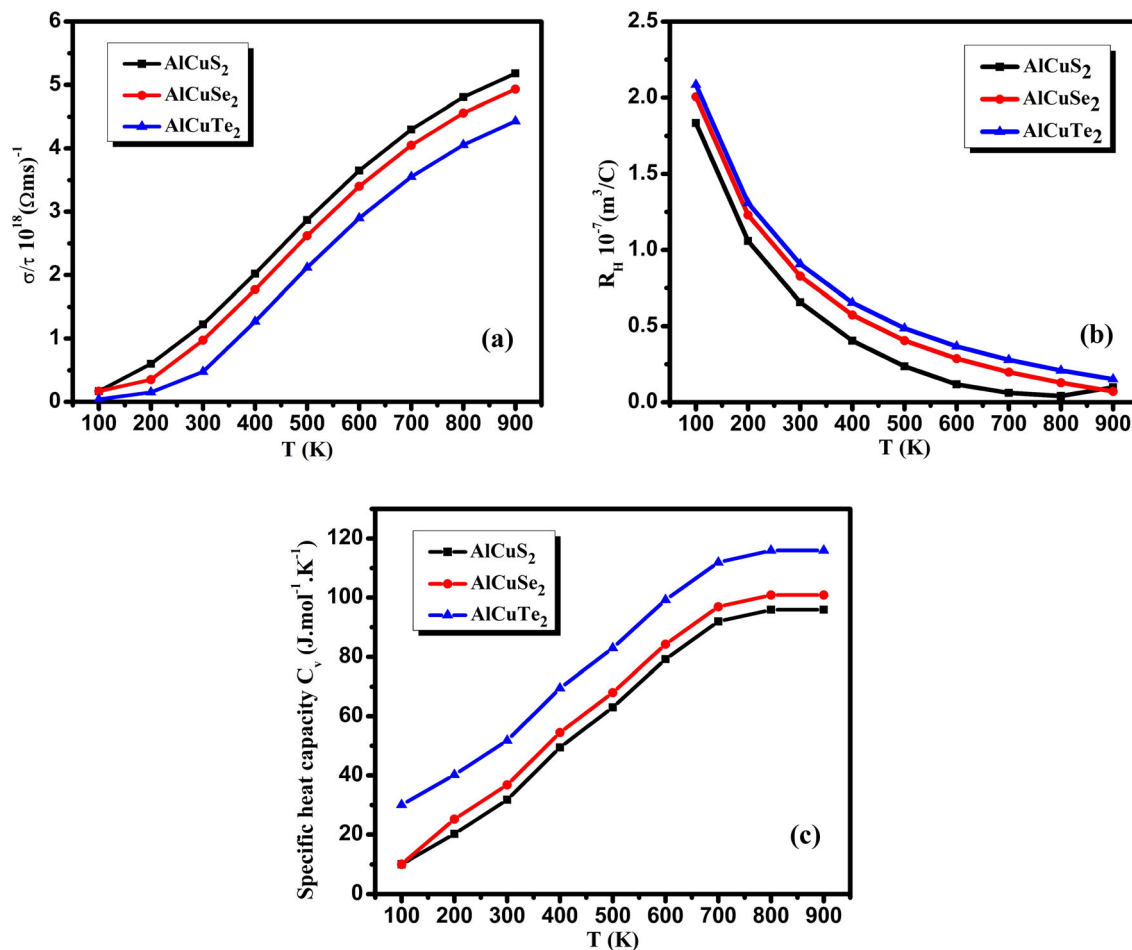


Figure 10 Calculated **a** electrical conductivity, **b** hall coefficient, **c** specific heat capacity for AlCuX₂ (X = S, Se, Te) compounds.

to be constant at high temperature values. According to these findings, AlCuX₂ (X = S, Se) alloys are better suited for thermoelectric applications such as thermoelectric generators. The analysis result of optical and thermoelectric properties has also indicated that AlCuS₂ and AlCuSe₂ are extremely efficient materials because of their absorption maximum functionality in the near ultraviolet region of solar energy. As a result of their absorption capacity, they are appropriate and promising alternatives for photovoltaic field. The AlCuTe₂ is best suited for thermoelectric applications and also can be significant for optoelectronic applications.

Conclusion

To conclude, we presented a first-principles study of novel ternary chalcopyrite structures using the FP-LAPW approach implemented in the wien2k code in

the context of density functional theory (DFT). The potential for exchange and correlation has been realized within the framework of the GGA-PBE approximation. The approximation recently developed by Becke–Johnson (mBJ modified Becke–Johnson) was also applied to improve the values of electronic properties and energy gaps of AlCuX₂ (X = S, Se, Te) compounds. The results obtained, from the calculation of the structural properties, show that the lattice parameter, for the tested compounds, is in excellent agreement with the results of experimental values. The high values of the modulus of compressibility (*B*) can be the cause of high stiffness and stability of the studied materials. The calculated band gap for AlCuS₂, AlCuSe₂, and AlCuTe₂ has in common the direct character of their band gap in gamma direction, with values of 2.78 eV, 2.30 eV, and 1.95 eV, respectively. The obtained findings show that these studied systems have an identical band structure, with the band gap decreasing from S

to Te. As a result, in all materials, the anion (X) has played an important role in designing the electronic band gap via valence electron contribution. Nevertheless, the optimized structural parameters, refractive index and the maximum of dielectric functions increase in the same order. Additionally, the refractive index, static dielectric constant, and reflectivity coefficient of this category of compounds increased from S to Te. The optical properties of these compounds, including their dielectric constant, absorption coefficient, and reflectivity, reveal that absorption increases in the visible range, notably for AlCuTe₂. Furthermore, because of the low thermal conductivity combined with the high electrical conductivity Seebeck coefficient, the calculated Figure of merit ZT for AlCuS₂ appears to be high. For the reason, the AlCuX₂ (X = S, Se, and Te) compounds have excellent physical properties that qualify these compounds for photovoltaic and thermoelectric applications. As a result, this research will assist experimental researchers in establishing a new advanced ternary chalcopyrite structure with excellent properties for the manufacturing of solar cells.

Data and code availability

Not Applicable.

Declarations

Conflict of interest The authors have no conflicts of interest to declare.

Ethical approval Not Applicable.

References

- [1] Gong Y, Zhu Q, Li B et al (2022) Elemental de-mixing-induced epitaxial kesterite/CdS interface enabling 13%-efficiency kesterite solar cells. *Nat Energy* 7:966–977. <https://doi.org/10.1038/s41560-022-01132-4>
- [2] Yuan Y, Zhu X, Zhou Y et al (2021) Pressure-engineered optical properties and emergent superconductivity in chalcopyrite semiconductor ZnSiP₂. *NPG Asia Mater* 13:15. <https://doi.org/10.1038/s41427-021-00285-0>
- [3] Hashemi M, Saki Z, Dehghani M et al (2022) Effect of transparent substrate on properties of CuInSe₂ thin films prepared by chemical spray pyrolysis. *Sci Rep* 12:14715. <https://doi.org/10.1038/s41598-022-18579-w>
- [4] Breeze P (ed) (2019) Solar power. In: Power generation technologies. Elsevier, pp 293–321
- [5] Martí A, Marrón DF, Luque A (2008) Evaluation of the efficiency potential of intermediate band solar cells based on thin-film chalcopyrite materials. *J Appl Phys* 103:073706. <https://doi.org/10.1063/1.2901213>
- [6] Mondal G, Santra A, Jana S et al (2018) Enhanced photocatalytic activity of ternary CuInS₂ nanocrystals synthesized from the combination of a binary Cu(I)S precursor and InCl₃. *J Nanoparticle Res* 20:108. <https://doi.org/10.1007/s11051-018-4213-7>
- [7] Xie H, Hao S, Bailey TP et al (2021) Ultralow thermal conductivity in diamondoid structures and high thermoelectric performance in (Cu_{1-x}Ag_x)(In_{1-y}Ga_y)Te₂. *J Am Chem Soc* 143:5978–5989. <https://doi.org/10.1021/jacs.1c01801>
- [8] Megag N, Ibrir M, Hadjab M et al (2021) Band parameters and thermoelectric properties of chalcopyrite ternary compounds Cd_xP₂ (X=Si, Ge and Sn). *Comput Condens Matter* 28:e00577. <https://doi.org/10.1016/j.cocom.2021.e00577>
- [9] Salman Khan M, Gul B, Khan G et al (2021) Ab-initio study about the electronic, optical and thermoelectric nature of α-, β-, and γ-phases of CdS semiconductor: using the accurate m-BJ approach. *Phys Scr* 96:055803. <https://doi.org/10.1088/1402-4896/abe6bd>
- [10] Benaadad M, Nafidi A, Melkoud S et al (2021) First-principles investigations of structural, optoelectronic and thermoelectric properties of Cu-based chalcogenides compounds. *J Mater Sci* 56:15882–15897. <https://doi.org/10.1007/s10853-021-06325-y>
- [11] Koroleva LI, Zashchirinskii DM, Khapaeva TM et al (2011) Manganese-doped CdGeAs₂, ZnGeAs₂ and ZnSiAs₂ chalcopyrites: a new materials for spintronics. *J Magn Magn Mater* 323:2923–2928. <https://doi.org/10.1016/j.jmmm.2011.05.054>
- [12] Łażewski J, Jochym PT, Parlinski K (2002) Band structure, born effective charges, and lattice dynamics of CuInS₂ from ab initio calculations. *J Chem Phys* 117:2726–2731. <https://doi.org/10.1063/1.1489993>
- [13] Wei J, Yang L, Ma Z et al (2020) Review of current high-ZT thermoelectric materials. *J Mater Sci* 55:12642–12704. <https://doi.org/10.1007/s10853-020-04949-0>
- [14] Laksari S, Chahed A, Abbouni N et al (2006) First-principles calculations of the structural, electronic and optical properties of CuGaS₂ and AgGaS₂. *Comput Mater Sci* 38:223–230. <https://doi.org/10.1016/j.commatsci.2005.12.043>
- [15] Lincot D, Guillemoles JF, Taunier S et al (2004) Chalcopyrite thin film solar cells by electrodeposition. *Sol Energy* 77:725–737. <https://doi.org/10.1016/j.solener.2004.05.024>

- [16] Maeda T, Wada T (2010) Electronic structure and characteristics of chemical bonds in CuInSe_2 , CuGaSe_2 , and CuAlSe_2 . *Jpn J Appl Phys* 49:04DP07. <https://doi.org/10.1143/JJAP.49.04DP07>
- [17] Omata T, Nose K, Otsuka-Yao-Matsuo S (2009) Size dependent optical band gap of ternary I-III-VI₂ semiconductor nanocrystals. *J Appl Phys* 105:073106. <https://doi.org/10.1063/1.3103768>
- [18] Chahed A, Benhelal O, Laksari S et al (2005) First-principles calculations of the structural, electronic and optical properties of AgGaS_2 and AgGaSe_2 . *Phys B Condens Matter* 367:142–151. <https://doi.org/10.1016/j.physb.2005.06.007>
- [19] Das S, Ranjan P, Gaurav K et al (2022) Structure, electronic and optical properties of chalcopyrite-type semiconducting materials XGaY_2 ($\text{X}=\text{Cu, Ag, Au}$; $\text{Y}=\text{S, Se, Te}$) for solar cell applications: a DFT study. *Phys B Condens Matter* 646:414305. <https://doi.org/10.1016/j.physb.2022.414305>
- [20] Okoli DN, Ekpunobi AJ, Okeke CE (2006) Optical properties of chemical bath deposited CuAlS_2 thin films. *Pac J Sci Technol* 7:59
- [21] Bharath Kumar Reddy Y, Sundara Raja V (2006) Preparation and characterization of $\text{CuIn}_{0.3}\text{Al}_{0.7}\text{Se}_2$ thin films for tandem solar cells. *Sol Energy Mater Sol Cells* 90:1656–1665. <https://doi.org/10.1016/j.solmat.2005.09.002>
- [22] Perng D-C, Kao T-T, Chang R-P (2014) Formation of wide band-gap CuInAlS_2 thin film and its application to UV detectors. *Thin Solid Films* 572:28–32. <https://doi.org/10.1016/j.tsf.2014.08.016>
- [23] Ikeda S, Nakamura T, Lee SM et al (2010) Photoreduction of water by using modified CuInS_2 electrodes. *Chemosuschem*. <https://doi.org/10.1002/cssc.201000169>
- [24] Marsen B, Cole B, Miller EL (2008) Photoelectrolysis of water using thin copper gallium diselenide electrodes. *Sol Energy Mater Sol Cells* 92:1054–1058. <https://doi.org/10.1016/j.solmat.2008.03.009>
- [25] Wang C-H, Cheng K-W, Tseng C-J (2011) Photoelectrochemical properties of AgInS_2 thin films prepared using electrodeposition. *Sol Energy Mater Sol Cells* 95:453–461. <https://doi.org/10.1016/j.solmat.2010.08.030>
- [26] Sun J, Chen G, Xiong G et al (2013) Hierarchical microarchitectures of $\text{AgGa}_{1-x}\text{In}_x\text{S}_2$: long chain alcohol assisted synthesis, band gap tailoring and photocatalytic activities of hydrogen generation. *Int J Hydrogen Energy* 38:10731–10738. <https://doi.org/10.1016/j.ijhydene.2013.02.138>
- [27] Huang D, Ju Z, Ning H et al (2014) First-principles study on CuAlTe_2 and AgAlTe_2 for water splitting. *Mater Chem Phys* 148:882–886. <https://doi.org/10.1016/j.matchemphys.2014.08.065>
- [28] Bafekry A, Faraji M, Fadlallah MM et al (2022) Ab-initio-driven prediction of puckered penta-like PdPSeX ($\text{X}=\text{O, S, Te}$) Janus monolayers: study on the electronic, optical, mechanical and photocatalytic properties. *Appl Surf Sci* 582:152356. <https://doi.org/10.1016/j.apsusc.2021.152356>
- [29] Bafekry A, Fadlallah MM, Faraji M et al (2022) Two-dimensional penta-like PdPSe with a puckered pentagonal structure: a first-principles study. *Phys Chem Chem Phys* 24:9990–9997. <https://doi.org/10.1039/D1CP04328E>
- [30] Bafekry A, Faraji M, Fadlallah MM et al (2022) Biphenylene monolayer as a two-dimensional nonbenzenoid carbon allotrope: a first-principles study. *J Phys Condens Matter* 34:015001. <https://doi.org/10.1088/1361-648X/ac2a7b>
- [31] Mardirossian N, Head-Gordon M (2017) Thirty years of density functional theory in computational chemistry: an overview and extensive assessment of 200 density functionals. *Mol Phys* 115:2315–2372. <https://doi.org/10.1080/00268976.2017.1333644>
- [32] Kiely E, Zwane R, Fox R et al (2021) Density functional theory predictions of the mechanical properties of crystalline materials. *CrystEngComm* 23:5697–5710. <https://doi.org/10.1039/d1ce00453k>
- [33] Petersen M, Wagner F, Hufnagel L et al (2000) Improving the efficiency of FP-LAPW calculations. *Comput Phys Commun* 126:294–309. [https://doi.org/10.1016/S0010-4655\(99\)00495-6](https://doi.org/10.1016/S0010-4655(99)00495-6)
- [34] He-Gen Z, Hong C, Dong C et al (2011) Electronic structures and optical properties of CuAlX_2 ($\text{X}=\text{S, Se, Te}$) semiconductors with a chalcopyrite structure. *Acta Physico-Chimica Sin* 27:2805–2813
- [35] Shirakata S, Chichibu S, Matsumoto S, Isomuraod S (1993) Photorefectance study of CuAlSe_2 heteroepitaxial layers. *Jpn J Appl Phys* 32:L167–L169. <https://doi.org/10.1143/JJAP.32.L167>
- [36] Zhang XZ, Shen KS, Jiao ZY, Huang XF (2013) A study of the electronic structures and optical properties of CuXTe_2 ($\text{X}=\text{Al, Ga, In}$) ternary semiconductors. *Comput Theor Chem* 1010:67–72. <https://doi.org/10.1016/j.comptc.2013.02.002>
- [37] Jaffe JE, Zunger A (1984) Theory of the band-gap anomaly in ABC₂ chalcopyrite semiconductors. *Phys Rev B* 29:1882–1906
- [38] Zhan Y, Pang M, Wang H, Du Y (2012) The structural, electronic, elastic and optical properties of $\text{AlCu}(\text{SeI}-\text{Te})_2$ compounds from first-principle calculations. *Curr Appl Phys* 12:373–379. <https://doi.org/10.1016/j.cap.2011.07.032>
- [39] Jain A, Ong SP, Hautier G et al (2013) Commentary: the materials project: a materials genome approach to accelerating materials innovation. *APL Mater* 1:011002. <https://doi.org/10.1063/1.4812323>

- [40] Rugut E, Joubert D, Jones G (2021) First principle studies on lattice thermal conductivity and thermoelectric properties of $\text{ScCu}(\text{S}, \text{Se}, \text{Te})_2$. *Mater Today Commun* 26:101905. <https://doi.org/10.1016/j.mtcomm.2020.101905>
- [41] Li S, Ma R, Zhang X et al (2017) Copper yttrium selenide: a potential photovoltaic absorption material for solar cells. *Mater Des* 118:163–167. <https://doi.org/10.1016/j.matdes.2017.01.037>
- [42] Bafekry A, Naseri M, Faraji M et al (2022) Theoretical prediction of two-dimensional BC_2X ($\text{X}=\text{N}, \text{P}, \text{As}$) monolayers: ab initio investigations. *Sci Rep* 12:22269. <https://doi.org/10.1038/s41598-022-26805-8>
- [43] Faraji M, Bafekry A, Fadlallah MM et al (2022) Two-dimensional XY monolayers ($\text{X}=\text{Al}, \text{Ga}, \text{In}$; $\text{Y}=\text{N}, \text{P}, \text{As}$) with a double layer hexagonal structure: a first-principles perspective. *Appl Surf Sci* 590:152998. <https://doi.org/10.1016/j.apsusc.2022.152998>
- [44] Bafekry A, Fadlallah MM, Faraji M et al (2022) Puckered penta-like PdPX ($\text{X}=\text{O}, \text{S}, \text{Te}$) semiconducting nanosheets: first-principles study of the mechanical, electro-optical, and photocatalytic properties. *ACS Appl Mater Interfaces* 14:21577–21584. <https://doi.org/10.1021/acsmi.1c23988>
- [45] Becke AD (2014) Perspective: fifty years of density-functional theory in chemical physics. *J Chem Phys* 140:18A301. <https://doi.org/10.1063/1.4869598>
- [46] Terki R, Feraoun H, Bertrand G, Aourag H (2004) Full potential linearized augmented plane wave investigations of structural and electronic properties of pyrochlore systems. *J Appl Phys* 96:6482–6487. <https://doi.org/10.1063/1.1789272>
- [47] Absike H, Hajji M, Labrim H et al (2019) Electronic, electrical and optical properties of Ag doped CuO through modified Becke–Johnson exchange potential. *Superlattices Microstruct* 127:128–138. <https://doi.org/10.1016/j.spmi.2017.12.038>
- [48] Blaha P, Schwarz K, Tran F et al (2020) WIEN2k: An APW+lo program for calculating the properties of solids. *J Chem Phys* 10(1063/1):5143061
- [49] Filippi C, Gonze X, Umrigar CJ (1996) Generalized gradient approximations to density functional theory: comparison with exact results. Elsevier, Amsterdam, pp 295–326
- [50] Camargo-Martínez JA, Baquero R (2012) Performance of the modified Becke–Johnson potential for semiconductors. *Phys Rev B Condens Matter Mater Phys* 86:1–8. <https://doi.org/10.1103/PhysRevB.86.195106>
- [51] Khalil RMA, Hussain F, Hussain MI et al (2020) The investigation of optoelectronic, magnetic and dynamical properties of Ce and Ti doped 2D blue phosphorene: a dispersion corrected DFT study. *J Alloys Compd* 827:154255. <https://doi.org/10.1016/j.jallcom.2020.154255>
- [52] Kaleemullah NS, Thangavel R, Kumar J (2021) Theoretical investigation on the electronic and optical properties of BSTS compounds with SOC and TB_mBJ potentials. *Bull Mater Sci*. <https://doi.org/10.1007/s12034-021-02352-2>
- [53] Sakuntala T, Arora AK (1996) Pressure-tuned resonance Raman scattering in AgGaSe_2 . *Phys Rev B* 53:15667–15674. <https://doi.org/10.1103/PhysRevB.53.15667>
- [54] Murnaghan FD (1944) The compressibility of media under extreme pressures. *Proc Natl Acad Sci* 30:244–247. <https://doi.org/10.1073/pnas.30.9.244>
- [55] Koller D, Tran F, Blaha P (2011) Merits and limits of the modified Becke–Johnson exchange potential. *Phys Rev B Condens Matter Mater Phys* 83:1–10. <https://doi.org/10.1103/PhysRevB.83.195134>
- [56] Jones RO, Gunnarsson O (1989) The density functional formalism, its applications and prospects. *Rev Mod Phys* 61:689–746. <https://doi.org/10.1103/RevModPhys.61.689>
- [57] Penn DR (1962) Wave-number-dependent dielectric function of semiconductors. *Phys Rev* 128:2093–2097. <https://doi.org/10.1103/PhysRev.128.2093>
- [58] Reddy RR, Ahammed YN, Reddy CVK, Buddhudu S (1996) A Simple model for evaluation of electronic polarizabilities of chalcopyrite semiconductors. *Cryst Res Technol* 31:827–830. <https://doi.org/10.1002/crat.2170310619>
- [59] Márquez R, Rincón C (1995) On the dielectric constants of AIBIIIC2VI chalcopyrite semiconductor compounds. *Phys status solidi* 191:115–119. <https://doi.org/10.1002/pssb.2221910112>
- [60] Madsen GKH, Carrete J, Verstraete MJ (2018) BoltzTraP2, a program for interpolating band structures and calculating semi-classical transport coefficients. *Comput Phys Commun* 231:140–145. <https://doi.org/10.1016/j.cpc.2018.05.010>
- [61] Singh J (ed) (2004) Boltzmann transport theory. In: *Modern physics for engineers*. Wiley, pp 353–363
- [62] Benaadad M, Nafidi A, Melkoud S et al (2022) Investigation of structural, optoelectronic and thermoelectric properties of GaCuX_2 ($\text{X}=\text{S}, \text{Se}$ and Te) chalcopyrites semiconductors using the accurate mBJ approach. *Phys B Phys Condens Matter*. <https://doi.org/10.1016/j.physb.2022.414118>
- [63] Gombia E, Leccabue F, Pelosi C (1984) The CVD growth of CuAlTe_2 single crystals. *Mater Lett* 2:429–431. [https://doi.org/10.1016/0167-577X\(84\)90155-1](https://doi.org/10.1016/0167-577X(84)90155-1)
- [64] Reshak AH (2015) Transport properties of mixed $\text{CuAl}(\text{S}_{1-x}\text{Se}_x)_2$ as promising thermoelectric crystalline materials. *J Phys Chem Solids* 78:46–52. <https://doi.org/10.1016/j.jpcs.2014.10.015>
- [65] Rabina O, Lin Y-M, Dresselhaus MS (2001) Anomalously high thermoelectric figure of merit in $\text{Bi}_{1-x}\text{Sb}_x$ nanowires by

- carrier pocket alignment. *Appl Phys Lett* 79:81–83. <https://doi.org/10.1063/1.1379365>
- [66] Takeuchi T (2009) Conditions of electronic structure to obtain large dimensionless figure of merit for developing practical thermoelectric materials. *Mater Trans* 50:2359–2365. <https://doi.org/10.2320/matertrans.M2009143>
- [67] Aliabad HAR, Rabbanifar S, Khalid M (2019) Structural, optoelectronic and thermoelectric properties of FeSb₂ under pressure: bulk and monolayer. *Phys B Condens Matter* 570:100–109. <https://doi.org/10.1016/j.physb.2019.06.001>

Publisher's Note Springer Nature remains neutral with regard to jurisdictional claims in published maps and institutional affiliations.

Springer Nature or its licensor (e.g. a society or other partner) holds exclusive rights to this article under a publishing agreement with the author(s) or other rightsholder(s); author self-archiving of the accepted manuscript version of this article is solely governed by the terms of such publishing agreement and applicable law.